

CD-NGP: A Fast Scalable Continual Representation for Dynamic Scenes

Zhenhuan Liu,  Shuai Liu, Zhiwei Ning, Jie Yang and Wei Liu

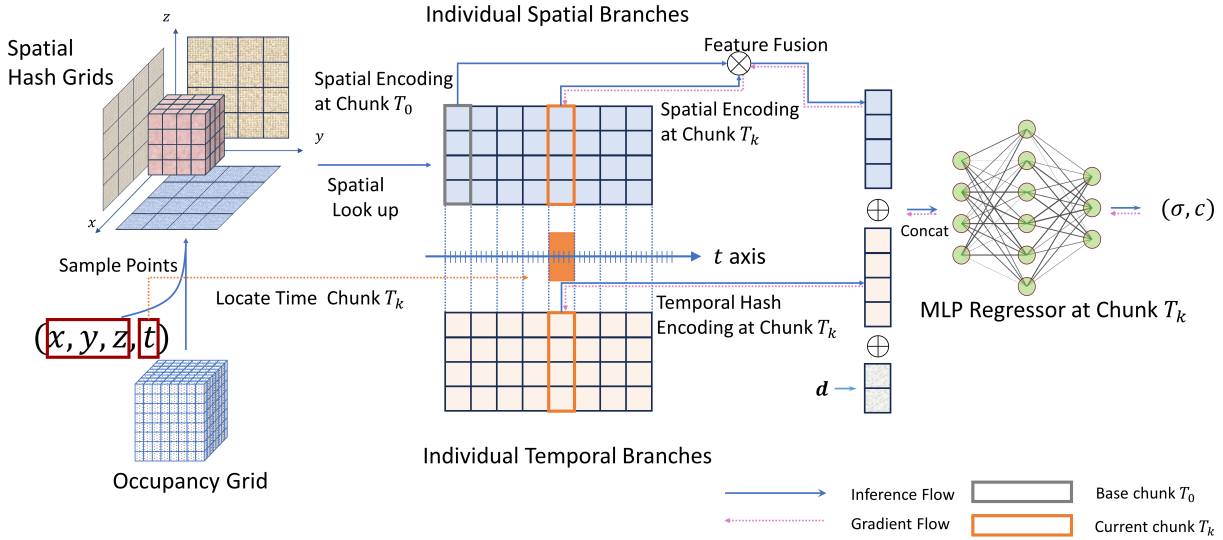


Fig. 1: The demonstration of our continual learning pipeline for dynamic scenes. Our method segments input videos into multiple chunks, train the model chunk by chunk and leverage the re-use of parameters from the first branch to ensure high scalability. The spatial hash features could be encoded along voxels, orthogonally projected planes or both.

Abstract—

Current methodologies for novel view synthesis (NVS) in dynamic scenes encounter significant challenges in harmonizing memory consumption, model complexity, training efficiency, and rendering fidelity. Existing offline techniques, while delivering high-quality results, are often characterized by substantial memory demands and limited scalability. In contrast, online methods grapple with the challenge of balancing rapid convergence with model compactness. To address these issues, we propose continual dynamic neural graphics primitives (CD-NGP). Our approach synergizes features from both temporal and spatial hash encodings to achieve high rendering quality, employs parameter reuse to enhance scalability, and leverages a continual learning framework to mitigate memory overhead. Furthermore, we introduce a novel dataset comprising multi-view, exceptionally long video sequences with substantial rigid and non-rigid motion, thereby substantiating the scalability of our method.

We evaluate the quality, speed and scalability our method on both established public datasets and our exceptionally long video dataset. Notably, our method achieves an 85% reduction in training memory consumption (less than 14GB) compared to offline techniques and significantly lowers streaming bandwidth requirements (less than 0.4MB/frame) relative to other online alternatives. The experimental results on our long video sequences dataset show the superior scalability and quality compared to existing state-of-the-art approaches.

Index Terms—Continual learning, Dynamic novel view synthesis, Neural Radiance Field.

1 INTRODUCTION

Neural radiance field (NeRF) [30] has made significant progress in 3D scene reconstruction and novel view synthesis. It takes multi-view RGB images with their camera poses as input and leverages multi-layer perceptrons (MLPs) to reconstruct both the geometry and color of the scene. Many variants have been proposed to improve NeRF’s efficiency [9, 31, 38, 53, 56], reconstruction quality [2–4], scalability [47, 50], and pose robustness [5, 13, 26, 32, 51, 52]. Recently, 3D Gaussian Splatting

(3DGS) [22] proposes an explicit representation with differentiable rendering, which significantly speeds up the reconstruction and enables real-time novel view synthesis. Despite significant progress having been made in this field, the above-mentioned methods assume that the scene is static and may not work properly in dynamic scenes.

To address the dynamic reconstruction problem, a number of efforts have been made in the offline setting, requiring access to the entire dataset during the training stage. For example, the methods in [15, 28, 29, 33, 34, 36, 44] propose to use MLP-based representation and achieve high-quality results. There are also methods speed up the optimization by using tensor factorization ([7, 17, 40]) and voxel representation [16, 45]. The more recent continual-learning-based methods [27, 48] can train models frame by frame, and streamable representations [43] enable the model to be loaded on the fly at inference. However, the offline methods require huge host memory *e.g.*, taking more than 100GB when reconstructing multi-view dynamic videos of 300 frames, and the continual learning-based methods are weak in

- Zhenhuan Liu is in Shanghai Jiao Tong University. E-mail: pignfan_zhilu_law268@sjtu.edu.cn
- Wei Liu is in Shanghai Jiao Tong University. E-mail: weiluvcv@sjtu.edu.cn.

Manuscript received xx xxx. 201x; accepted xx xxx. 201x. Date of Publication xx xxx. 201x; date of current version xx xxx. 201x. For information on obtaining reprints of this article, please send e-mail to: reprints@ieee.org.
Digital Object Identifier: xx.xxx/TVCG.201x.xxxxxxx

balancing the convergence speed and model compactness. As a result, these methods are limited in scalability, making them unsuitable for long videos.

In this paper, we propose *continual dynamic neural graphics primitives* (CD-NGP), a fast and scalable representation for reconstructing dynamic scenes, which enables dynamic reconstruction in long videos.

The proposed methodology is illustrated in Fig. 1: we partition dynamic videos into multiple segments based on timestamps and perform reconstruction using distinct model branches. Each branch includes MLP regressors, spatial hash encoding for spatial coordinates (x, y, z) , and temporal hash encoding for the timestamp t . For the first segment, we encode spatial features using a large hash table, and for subsequent segments, we use a smaller hash table. By reusing parameters from the initial branch, we enhance scalability and accelerate convergence. For each segment, we identify the corresponding model branch, sample 3D points (x, y, z) according to frame pixels and cached occupancy grids [31], and represent spatial features using spatial hash grids. The spatial features from the initial branch and the current branch are fused through element-wise summation by default or concatenation if applicable. Temporal features are encoded by the hash table for the timestamp t within the current branch only. These spatial and temporal features, along with the viewing direction d , are concatenated and input into MLP regressors for rendering and optimization.

We validate the effectiveness of our method through comprehensive experimental results on both the widely used public datasets and the dataset proposed by us. As illustrated in Fig. 2, our method reaches a new balance between rendering quality, model size, and training time while remaining memory-friendly, in which we use metrics on the *flame salmon* scene in the DyNeRF dataset for fair comparison. The perceptual consistency is measured by 1 – LPIPS by AlexNet [24, 57], and the speed is the reciprocal of the training time. The compactness and RAM-Efficiency are mapped by $-\log$ function from the model size and memory occupation respectively.

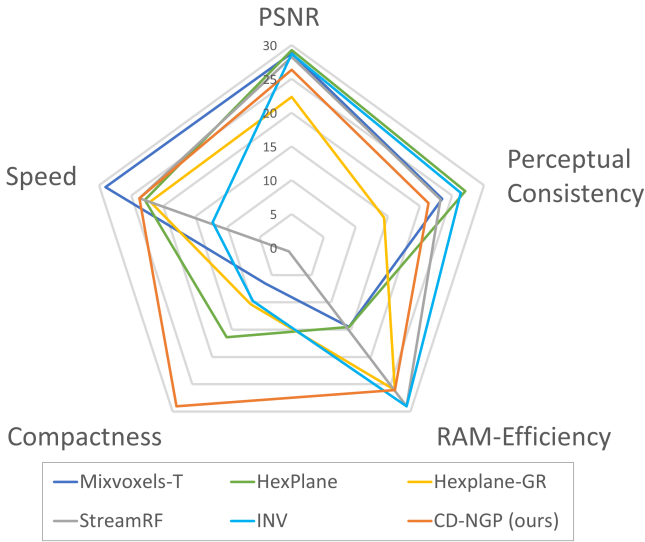


Fig. 2: Comparison between different performance indexes of our method and recent representative baselines.

Compared with prevailing offline baselines, our method consumes 85% less host memory at the training phase, 40% less model size at the inference phase, and delivers comparable results. Compared with online baselines, our method achieves compact model size, high quality, and fast convergence simultaneously. Contributions of this paper are three-fold as follows:

- We propose a novel method combining spatial and temporal hash encodings for dynamic scenes and yield comparable results to both offline and online methods.

- We propose a fast continual learning framework for dynamic scenes and reduce memory and storage occupation significantly.
- We provide a dataset of multi-view long video sequences (> 3 minutes) with large motion and further demonstrate the scalability of our method on the proposed dataset.

2 RELATED WORK

2.1 Fast novel view synthesis in static scenes

The acceleration of NeRFs falls into two categories: training acceleration and rendering acceleration. Plenoxels [18] uses voxel grids to represent the scene and achieves magnitudes of acceleration over MLP backbones. TensorRF [9] decomposes the 3D scene as the product of tensors and achieves fast novel view synthesis. Plane-based methods [17, 21] project 3D points onto 3 orthogonal 2D planes to ensure sparsity and achieve fast convergence. KiloNeRF [37] leverages an occupancy grid and a multi-resolution hash encoding along with optimized tiny MLPs to enable fast novel view synthesis within a minute. The recent 3D Gaussian method [22] represents the scenes as a union of explicit Gaussian point clouds and achieves high fidelity, fast convergence, and real-time rendering on high-end hardware by eliminating the querying burden of spatial representations. Instant-NGP [31] distills the large MLP in NeRF [30] into tiny MLPs to accelerate rendering by thousands of times. Hedman *et al.* [20] propose the *baking* method (converting the MLP representation into explicit meshes) to accelerate the rendering process. They alpha-compose the cached features along the ray and use MLPs only once per ray to overcome the computation load of the per-point MLP querying in NeRF. BakedSDF [56] stores the view-dependent features into Gaussian spheres along the reconstructed surfaces, and achieves real-time rendering on ordinary laptops. MobileNeRF [10] represents scenes into meshes and enables real-time rendering on mobile devices. Light field methods [8, 19, 42] directly represent the scene as a set of rays to eliminate volume rendering and enable real-time applications on mobile devices.

2.2 Representations of dynamic scenes

There are mainly 3 variants of NeRF for dynamic scenes. The first class is pure MLP-based representation. D-NeRF [36] leverages a large *deformation* MLP to model the transition and the trajectories of the objects and extends NeRF to simulated dynamic scenes. DyNeRF [28] uses long latent vectors to encode temporal information along with large MLPs to achieve high-fidelity novel view synthesis in real dynamic scenes. Park *et al.* [34] propose an interpolation-based MLP representation for dynamic scenes and achieve significant acceleration over DyNeRF.

The second class is tensor factorization-based representation. HyperReel [1] proposes a network to predict the sample locations and represent dynamic scenes by key-frame-based TensorRF [9] representation to ensure high fidelity and real-time rendering without any custom CUDA kernels. K-Planes [17] and HexPlane [7] factorize the whole 4D field into the product of 2D planes. Though differently implemented, they both achieve high-fidelity results with intermediate model size (200MB) and training time (100 minutes) on the DyNeRF dataset. The third class is the explicit voxel-based representations. TineuVox [16] leverages the deformation MLP in D-NeRF and implements a 3D voxel grid with multi-scale interpolation. It achieves high fidelity and fast convergence on the D-NeRF dataset. MixVoxels [45] leverages the standard deviation across the time of all pixels to estimate a variation field to decompose the dynamic scene into static and dynamic voxels. Equipped with different representations for static and dynamic objects, MixVoxels achieves high-fidelity results and super-fast convergence (15 minutes) on DyNeRF dataset. Song *et al.* [43] train Instant-NGP [31] and TensorRF [9] offline and stream the models along the feature channels for dynamic scenes. Concurrent works are leveraging 4D Gaussian point clouds [49, 55] or 3D Gaussians with deformation networks [54] achieving real-time rendering and high fidelity in dynamic scenes.

2.3 Continual learning of NeRF

Continual learning (online learning) aims to adapt to new tasks while defying catastrophic forgetting (resisting performance downgrade on the previous tasks) [12]. There are mainly 3 approaches to achieving continual learning: replay, regularization, and parameter isolation. The replay-based methods either store the previous data in a buffer and replay them [39], or use the model to generate the pseudo-ground truth of previous tasks while training on new tasks [41]. The regularization-based methods hold the parameters close to the solution of previous tasks [14]. The parameter-isolation methods use different parameters to cope with different tasks. Recent efforts based on generative replay [6, 11, 35] enable continual learning of NeRF in static scenes and achieve high fidelity. StreamRF [27] applies continual NeRF to dynamic scenes by parameter isolation. Their explicit voxel representation enables fast reconstruction (75 minutes for 300 frames) and could be streamed frame by frame. INV [48] uses a shared color MLP and trains different structure MLPs frame by frame to form a continual NeRF representation and achieves high-fidelity results in dynamic scenes.

3 METHOD

3.1 Preliminaries

Inspired by the previous NeRF variants [7, 17, 28, 31, 36, 38, 45] and continual learning methods [6, 11, 27, 35, 43, 48], we focus on the dynamic novel view synthesis problem in the multi-view setting and solve the problem in a continual learning manner to alleviate the huge memory consumption and bandwidth costs.

Following previous methods [7, 17, 28, 36], we consider the dynamic scene as a set of 3D points $\mathbf{p} = (x, y, z)$ with optical attributes (σ, \mathbf{c}) , where σ is the volume density of the point and \mathbf{c} is the color of the point. We train our model along camera rays to reconstruct the scene. A camera ray is defined as:

$$\mathbf{r}(u) = \mathbf{o} + u\mathbf{d}, \quad (1)$$

where \mathbf{o} is the optical center of the camera, \mathbf{d} is the direction off the camera. For each point along the camera ray with coordinates (x, y, z) observed at direction $\mathbf{d} = (\phi, \psi)$, a field function F is queried to obtain the optical attributes (σ, \mathbf{c}) . Conditioned on time t , the entire model is defined as:

$$(\sigma, \mathbf{c}) = F_{\Theta}(x, y, z, t, \phi, \psi), \quad (2)$$

where the function F denotes the dynamic NeRF model and Θ denotes trainable model parameters.

Let I_i denote the i -th input image corresponding to the observation direction d_i , $\mathbf{V} = \{v_i \mid v_i = (I_i, d_i), 1 \leq i \leq N_{view}\}$ is the set of the training views, where $i, N_{view} \in \mathbb{Z}^+$. Let \mathbf{D}_a denote the readily-accessible data at one step. Previous methods [6, 35] for static scenes define the continual learning problem as learning a unified representation with a limited subset of views V_a available at every optimization step, *i.e.* $\mathbf{D}_a = V_a \subsetneq V$. However, a more natural definition of continual NeRF is in the dynamic scenes, where the observations at different time stamps arrive continually. Denoting all the time stamps as $\mathbf{T} = \{\tau_i \mid 1 \leq i \leq N_{time}\}$, $i, N_{time} \in \mathbb{Z}^+$, we define the continual learning problem as synthesizing a video sequence where the model could only have access to a limited number of frames $\mathbf{T}_a \subsetneq \mathbf{T}$ from all views \mathbf{V} at each step, *i.e.* $\mathbf{D}_a = \{\mathbf{V} \times \mathbf{T}_a\}$ where \times is the Cartesian product of sets.

To simplify the notations, let the whole sequence of frames be evenly divided into k chunks where a chunk $\mathbf{T}_k = \{\tau_i \mid \lfloor \frac{N_{time}}{k} \rfloor = k\}$ is a sequential subset of length T_{chunk} . We define the continual learning problem as learning a representation where only the frames in the current chunk are available at each optimization step, *i.e.* $\mathbf{T}_a = \mathbf{T}_k$. Accordingly, $T_{chunk} = 1$ denotes training the model online in a frame-by-frame manner, $T_{chunk} = 10$ denotes training the model online with a buffer of 10 frames. If the video contains 300 frames in total, the $T_{chunk} = 300$ denotes training the entire 300-frame sequence offline. The definition is close to real-world applications since caching all training frames in memory or storing them on the disk is limited in scalability for long videos.

3.2 Representation of short dynamic intervals

As shown in [46], naive 4D hash grids for dynamic scenes are short in reconstruction quality. To achieve fast reconstruction and slim model size simultaneously, we represent time and spatial features separately and concatenate them to alleviate feature confusion. The spatial hash features may be encoded along 3D voxels [31], 2D planes [17, 21], or both [38]. The time feature is encoded by short hash tables in a per-frame manner. Following previous state-of-the-art methods [16, 30, 31], we apply a two-fold field function for geometry and color individually. The architecture of the field function is thus defined as:

$$(\sigma, \mathbf{H}) = f_{\theta_1}(\Psi(\mathbf{x}) \oplus \Gamma(t)), \quad (3)$$

$$\mathbf{c} = f_{\theta_2}(\mathbf{H}, \phi, \psi). \quad (4)$$

where $\mathbf{x} = (x, y, z)$ is the spatial coordinates, $\Psi(\mathbf{x})$ denotes configurable spatial hash encodings, f_{θ_1} is a tiny MLP with trainable parameter θ_1 , $\Gamma(t)$ is the hash encoding for time axis alone, and \oplus is the concatenation of vectors. The MLP f_{θ_1} in Eq. (3) fuses features across the spatial domain and time domain and obtains the volume density σ . View-dependent colors \mathbf{c} are regressed by another tiny MLP with parameter θ_2 in Eq. (4). The spatial encoders $\Psi(x)$ follow a multi-resolution concatenated format, defined as:

$$\Psi(\mathbf{x}) = \bigoplus_{m=1}^L P_m(x, y, z) \quad (5)$$

where the $P_m(x, y, z) \in \mathbf{R}^F$ denotes the tri-linearly interpolated value from the nearby 8 grid vertices w.r.t. 3D coordinates (x, y, z) at the l -th resolution, L is the number of the resolutions, and F is the dimensions of features $P_m(x, y, z)$, which are similar to those in Instant-NGP [31]. If necessary, Eq. (5) could be adopted to the hybrid (MERF) representation [38], defined as:

$$\Psi(\mathbf{x}) = \bigoplus_{m=1}^L P_m(x, y, z) + Q_{mxy}(x, y) + Q_{myz}(y, z) + Q_{mzx}(z, x) \quad (6)$$

where $Q_{mij}(i, j)$ denotes the bi-linearly interpolated value from the 4 nearby vertices in the orthogonally projected planes w.r.t. axes (i, j) at the m -th resolution. Removing the $P_m(x, y, z)$ term leads to a pure plane representation like [17, 21].

3.3 Continual dynamic neural graphics primitives (CD-NGP)

Unlike the existing replay-based methods for static scenarios [6, 35], we solve the continual learning problem of dynamic novel view synthesis via parameter isolation. The current state-of-the-art methods by tensor factorization [7, 17] or explicit voxels [45] are regressions of the optical attributes in 3D space within a limited time instead of the object trajectory and inherent dynamics. Therefore, the replay method is of limited use in our defined scenario: Since new transient processes are constantly arriving, the model of a limited size is not capable of reconstructing unlimited transient effects. Thus, the replay-based method suffers from catastrophic forgetting.

To address this issue, we propose our *continual dynamic neural graphics primitives* (CD-NGP) based on parameter isolation. We split the model into N_{chunk} branches to represent different *chunks* of the dynamic scene accordingly. The k -th branch contains spatial hash encoder $\Psi_k(\mathbf{x})$, temporal hash encoder $\Gamma_k(t)$, and MLPs $f_{\theta_{1k}}, f_{\theta_{2k}}$. We train the first branch (*base branch*) with a large spatial hash table to better reconstruct the scenes with initial movements and static objects. Then we reuse the spatial features from the base branch and train the subsequent branches (*auxiliary branches*) to compensate for residuals. We thus substitute the $\Psi(\mathbf{x})$ in Eq. (3) with the fused feature to obtain the volume density σ at the k -th model branch under the continual learning setting as:

$$(\sigma, \mathbf{H}) = f_{\theta_{1k}}((\Psi_0(\mathbf{x}) + \Psi_k(\mathbf{x})) \oplus \Gamma_k(t)), \quad (7)$$

where $\Psi_0(\mathbf{x})$ denotes the spatial encoder of the base branch, $\Psi_k(\mathbf{x})$ denotes the spatial encoder of the current branch. The view-dependent colors are regressed as Eq. (4) with the color MLP f_{θ_k} . For simplicity, we denote the models adopting pure voxel encoders in Eq. (5) as CD-NGP, the models adopting the hybrid encoders in Eq. (6) as CD-MERF.

The scalability of our method derives from the redundancy of dynamic scenes and the flexibility of hash table sizes. As pointed out by [45], most points ($> 90\%$) in the dynamic scenes are static. We thus leverage the shared static points across time and represent the first chunk with a large hash table and the subsequent chunks with small hash tables to ensure scalability. To be specific, if we follow the default setting of Instant-NGP [31] and set the hash table in the first branch as 2^{P_1} , the sizes of hash tables in subsequent branches could be configured as 2^{P_2} . Please note that P_1 is significantly larger than P_2 to ensure the scalability of the model. When $(P_1, P_2) = (19, 14)$, the hash table in the second branch consumes only $1/32$ of the parameters in the first branch. Since the spatial hash tables occupy the most parameters in the model, and most chunks are encoded by the subsequent branches, our asymmetric hash table design enables continual learning of dynamic scenes and high scalability in streaming scenarios simultaneously. The total bandwidth consumption of our method is $\mathcal{O}(N_{chunk} \cdot 2^{P_2} LF + 2^{P_1} LF)$, while the previous method [43] requires offline training and consumes $\mathcal{O}(\mathbf{K} \cdot 2^{P_1} LF)$ bandwidth, where \mathbf{K} ranging from 0.5 to 16 is their bandwidth budget controlling the bitrates in streaming scenarios. If the bandwidth is extremely limited, the hash tables in our model could be arranged as a combination of 3D representations and 2D representations like [38] to reduce the bandwidth cost additionally.

3.4 Rendering and optimization

Given the sampled optical attributes on the rays in Eq. (1), we adopt volume rendering to get the 2D pixels, defined as:

$$\hat{C}(r) = \sum_{i=1}^N T_i \alpha_i \mathbf{c}_i = \sum_{i=1}^N T_i (1 - e^{-\sigma_i \delta_i}) \mathbf{c}_i, \quad (8)$$

where $T_i = \exp(-\sum_{j=1}^{i-1} \sigma_j \delta_j)$ denotes the transmittance, δ_i is the interval between neighboring samples, N is the number of samples along the ray. The model is optimized by L2 photometric loss with three regularization terms, defined as:

$$L = \frac{1}{|\mathbf{R}|} \sum_{r \in \mathbf{R}} \|C(r) - \hat{C}(r)\|_2^2 + \lambda_d L_d + \lambda_o L_o + \lambda_r L_r \quad (9)$$

Where \mathbf{R} denotes the set of the camera rays. L_d is the distortion loss in Mip-NeRF 360 [3], defined as:

$$L_d = \sum_{i,j} w_i w_j \left| \frac{s_i + s_{i+1}}{2} - \frac{s_j + s_{j+1}}{2} \right| + \frac{1}{3} \sum_i w_i^2 (s_{i+1} - s_i) \quad (10)$$

where s_i denotes the normalized ray distance along the ray, $w_i = T_i \alpha_i$ is the weight of the i -th sample.

L_o in Eq. (9) is the entropy on the opacity by [25], defined as:

$$L_o = -o \log(o), \quad o = \sum_{j=1}^N T_j \alpha_j. \quad (11)$$

L_r in Eq. (9) is the L1 regularization on the spatial features in the current branch as:

$$L_r = \|\Psi_k(\mathbf{x})\|_1. \quad (12)$$

We set λ_r as 0.001 to encourage leverage of the base hash encoder. Based on [25], we set a larger λ_d, λ_o as 0.005 to alleviate foggy effects.

3.5 Continual learning pipeline.

We further illustrate the whole process of our method in Algorithm 1, where η_{init} and η_{aux} denote the numbers of iterations of the initial branch and the auxiliary branches, respectively. $\Psi_i, \Gamma_i, \theta_1^{(i)}, \theta_2^{(i)}$ denote the model parameters in the branches. The whole model is trained chunk by chunk. The implementation will be available upon publication.

Algorithm 1 Continual learning pipeline

Require: $N_{chunk}, T_{chunk}, \eta_{init}, \eta_{aux}, \Psi_i, \Gamma_i, \theta_1^{(i)}, \theta_2^{(i)}, i \in \mathbb{N}$
Ensure: The whole representation for dynamic scenes.

```

1:  $k \leftarrow 0, T_{episode} \leftarrow 30$  % initialize
2: while  $k < N_{chunk}$  do
3:    $\mathbf{T}_a \leftarrow \mathbf{T}_k$  % assign the current chunk
4:    $\mathbf{D}_a \leftarrow \mathbf{V} \times \mathbf{T}_a$  % assign accessible data
5:   if  $k \bmod T_{episode} = 0$  then
6:      $\eta \leftarrow \eta_{init}$  % The first branch in the episode.
7:   else
8:      $\eta \leftarrow \eta_{aux}$  % The other branches in the episode.
9:      $\theta_1^{(k)}, \theta_2^{(k)}, \Gamma_k \leftarrow \theta_1^{(k-1)}, \theta_2^{(k-1)}, \Gamma_{k-1}$  % Initialize with the previous branch.
10:  end if
11:  Train the  $k$ -th model branch  $(\Psi_k, \Gamma_k, \theta_1^{(k)}, \theta_2^{(k)})$  for  $\eta$  steps.
12:   $k \leftarrow k + 1$  % update the chunk index  $k$ 
13: end while

```

4 EXPERIMENTS

4.1 Datasets

The DyNeRF dataset [28] is the most prevalent benchmark for dynamic view synthesis, providing high-quality multi-camera videos on which current state-of-the-art methods are primarily evaluated. This dataset includes six unique cooking scenes, each featuring varying illumination, food topological changes, and transient effects such as flames. It consists of five videos, each containing 300 frames, and one extended video with 1200 frames, captured at a resolution of 2704×2028 with up to 21 camera views at 30 frames per second (FPS). Following the approach of HexPlane [7], we excluded the unsynchronized scene *coffee martini* and conducted experiments on the remaining scenes, using the first 300 frames of the 1200-frame video *flame salmon* for evaluation.

Meetroom dataset [27] is another dataset for dynamic view synthesis that contains 3 scenes captured by 13 synchronized cameras at 1280×720 resolution. The lengths of the scenes are set as 300 frames and the refresh rates are set as 30 FPS.

To further validate the effectiveness of our method on long video sequences, we introduce a new dataset comprising 5 dynamic scenes at a resolution of 3840×2160 . Similar to the DyNeRF dataset [28], these scenes are captured by 20 GoPro cameras operating at 30 FPS. We synchronize the multi-view videos using environmental sound and incorporate chessboard images within the scenes to facilitate camera calibration and pose estimation.

The dynamics in our dataset are notably more challenging than those in the DyNeRF dataset, featuring significant non-rigid motions of human bodies and transient effects such as slide effects on the screens in the backgrounds. To comprehensively assess the scalability of our method, we provide 5 scenes with a duration exceeding 200 seconds (6000 frames), which is over 10 times longer than the previous DyNeRF dataset.

This dataset was meticulously collected to evaluate the scalability of our method and to support further research. We have carefully reviewed the videos to ensure they do not contain any controversial or offensive content before using them for research purposes. While the faces in the videos may contain identifiable information, this information will be used solely for research and will not be disclosed to any third party. All videos were collected with the explicit consent of all participants. The view in the upper center is designated for validation.

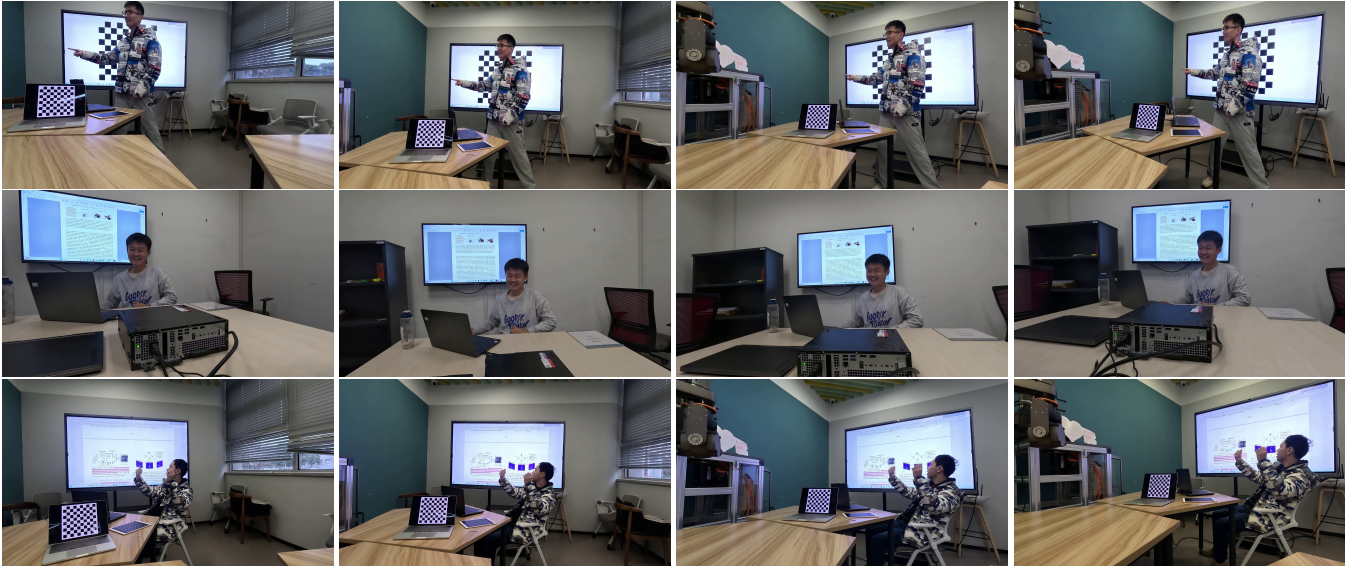


Fig. 3: Example frames sampled from the proposed long multi-view video dataset.

4.2 Implementation details

Our implementation is based on HexPlane [7], Instant-NGP [31], and NGP-pl [25]. All the metrics are measured on a single RTX 3090 GPU if not otherwise specified. Similar to the previous work [7, 28], we select the view in the center with index 0 for evaluation on both datasets. Following most of the state-of-the-art methods [17, 27, 28, 43, 45] we train and evaluate the model at resolution 1352×1014 on the DyNeRF dataset. We use 1280×720 resolution for our dataset to fit into memory. We use the importance sampling scheme in [28] at a batch size of 1024 rays. The parameters are optimized by Adam [23], with $\epsilon = 10^{-15}$, $\beta = (0.9, 0.96)$. The learning rate is set as 0.001 and scheduled by cosine function following [25]. We set the size of the hash table in the first branch as 2^{19} and the size of the hash table in the subsequent branches as 2^{14} , and we set the structural parameters (L, F) in the spatial hash encoders as $(12, 2)$ if not otherwise specified. Following MERF [38] for static scenes, we use a smaller hash table for the hybrid representation in Eq. (6) than pure voxel hash grid [31] representation in Tab. 3 to ensure the compactness and scalability of our method. Denoting the lengths of hash tables along pure voxels in a branch of CD-NGP as 2^P , the lengths of hash tables in the CD-MERF are set as 2^{P-3} and 2^{P-4} for voxel and plane encoders respectively. The number of the parameters of the MERF representation is thus reduced to $1 - 2^{-3} - 3 \times 2^{-4} = 31.25\%$ of the voxel hash grids. Since the hash tables take up the majority of the parameters, the model size is reduced from $21M$ to $7.5M$ as in Tab. 3.

At the base branch, we initialize the models and train for 18k iterations, and for each of the subsequent branches we train for 3k iterations using the previous branch for initialization. We use LeakyReLU activation in the MLP regressors. For long video sequences, we assign 30 chunks as an *episode*. The MLP regressors are re-trained from initialization in the first branch of each episode to adapt to recent changes. Strategies for updating the occupancy grids are identical with [31]. To save storage, we use only one shared occupancy grid for all the branches. We report the model sizes with the occupancy grid under bfloat16 precision and parameters in float32 precision.

We set the dimensions of the latent feature \mathbf{H} in Eq. (3) as 48. We use MLPs with two hidden layers and the dimensions of the hidden layers in Eqs. (3) and (4) are set as 128, and 64 respectively. We use MLPs with identical structures for different branches. We set the resolutions of the hash encoders of the CD-NGP within $(16, 2048)$ times the scale of the scene, and we use $(64, 2048)$ for the plane representation.

4.3 Results and comparisons

4.3.1 DyNeRF dataset.

Table 1 shows the quantitative comparisons between CD-NGP and other state-of-the-art methods on DyNeRF dataset. We use the officially released metrics. The methods in [28, 34] are trained on 8 V100 GPUs or equally 4 A100 GPUs. The methods in [28, 34, 43] have no official implementations available. We are unable to obtain the missing quality metrics in [17] because of their huge memory occupation in the default resolution. HexPlane [7] uses resolution $(1024, 768)$ in their implementation, so the memory occupation is much smaller than other offline methods. We use the official implementation of StreamRF [27] and INV [48] and report the average metrics on the 5 synchronized scenes of the dataset. StreamRF [27] and INV [48] are trained per-frame. NeRFplayer [43] is trained offline but streamable upon inference. 4DGS [55] caches the frames onto disk for training to alleviate memory occupation with a trade-off on training speed. The reconstruction quality is measured by PSNR, DSSIM, and LPIPS [57] (by AlexNet [24]) following common practices [7, 28, 45]. To prove the viability of our parameter-isolation-based method, we apply the previous state-of-the-art method *HexPlane* [7] to continual learning setting with parameter-regularization (*HexPlane-PR*) and generative replay (*HexPlane-GR*) as additional baselines.

We compare our method with both online and offline baselines. As demonstrated in Tab. 1, our CD-NGP is $32 \times$ faster than the MLP-based continual representation INV [48], $44 \times$ smaller than the voxel-based continual representation StreamRF [27] and significantly outperforms the two additional baselines in the continual learning setting. The undesirable results from HexPlane-PR and HexPlane-GR show the limitations of the regularization-based and replay-based methods in dynamic scenes: unlike the static scenes, the objects are not stationary across time and the models with limited complexity are not capable of reconstructing unlimited transient effects. Benefiting from the parameter isolation like StreamRF [27] and INV [48], our method achieves fast convergence and compact model size simultaneously. It leverages the hash tables to ensure fast convergence and reuses the features from differently-configured spatial hash tables to ensure high scalability. Compared with prevailing offline methods [7, 17, 28, 34, 45, 55], our method only requires caching $T_{chunk} = 10$ frames into buffer by continual learning and thus reduces memory occupation by 85%. Our method also achieves 40% less model size (0.4MB/frame) by leveraging the feature fusion of the *base* and the *auxiliary* branches with comparable quality.

Figure 4 provides qualitative comparisons. Compared with offline

Table 1: Comparisons between our CD-NGP and SOTA methods on the DyNeRF dataset. Memory denotes the maximum host memory required for training. - denotes the metrics unreported in the original publications. **Best**, **Second**, and **Third** metrics are in highlight. The *full model* of [27] results in much worse metrics than those reported in their paper, so we only report the metrics of their *pilot model*.

Method	Online	Offline	T_{chunk}	PSNR \uparrow	DSSIM \downarrow	LPIPS \downarrow	Time \downarrow	Size \downarrow	Memory \downarrow
DyNeRF † [28]		✓	300	29.58	0.020	0.083	7 days	28MB	>100GB
NeRF-T † [28]		✓	300	28.45	0.023	0.10	-	-	>100GB
Interp-NN [34]		✓	300	29.88	-	0.096	2 days	20MB	>100GB
HexPlane [7]		✓	300	31.57	0.016	0.089	96 min	200MB	62GB
K-Planes [17]		✓	300	31.63	-	-	110 min	200MB	>100GB
MixVoxels-T [45]		✓	300	30.71	0.024	0.162	15 min	500MB	>100GB
4DGS [55]		✓	300	32.01	-	0.055	6 hours	4000MB	<10GB
HyperReel [1]		✓	50	31.1	-	0.096	9 hours	360MB	18GB
NeRFplayer [43]		✓	300	30.29	-	0.152	5.5 hours	-	>100GB
StreamRF [27]	✓		1	28.85	0.042	0.253	75 min	5000MB	<10GB
HexPlane-PR	✓		10	24.03	0.081	0.244	100 min	318MB	14GB
HexPlane-GR	✓		10	25.17	0.050	0.272	125 min	318MB	14GB
INV [48]	✓		1	29.64	0.023	0.078	40 hours	336MB	<10GB
CD-NGP (Ours)	✓		10	30.23	0.029	0.198	75 min	113MB	14GB

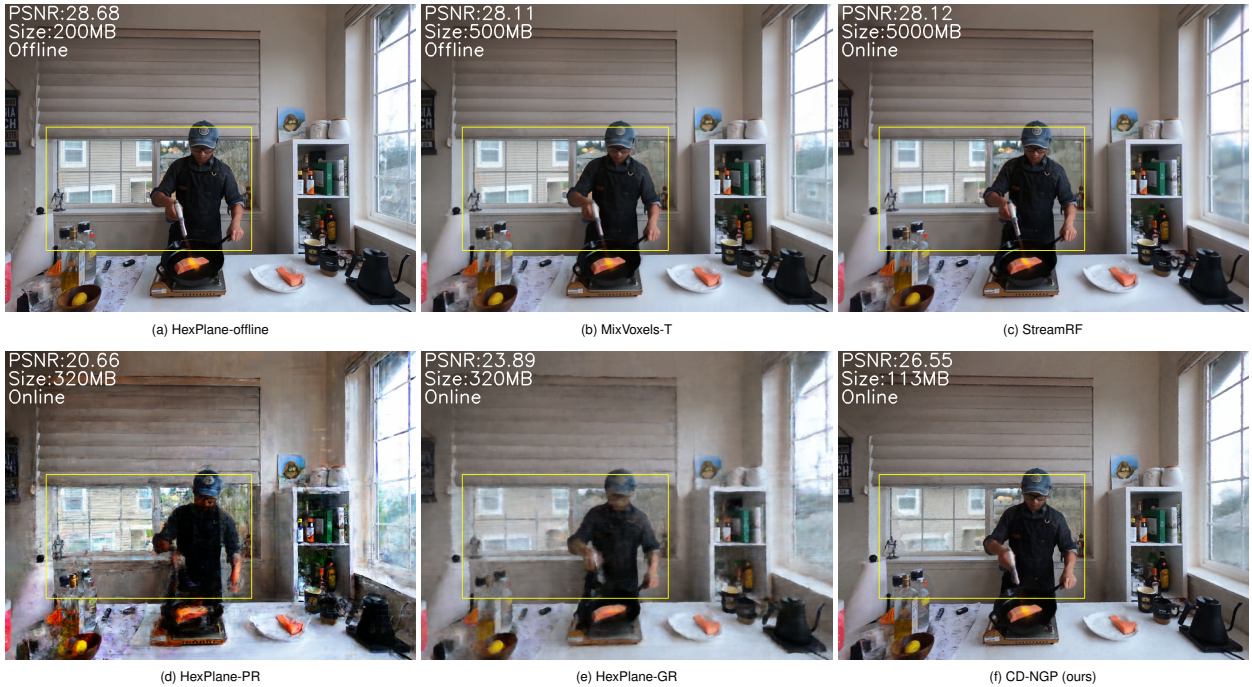


Fig. 4: Comparison of reconstruction quality on the most challenging *flame salmon* scene in DyNeRF dataset. PSNRs are computed under the resolution 1352×1014 .

methods in Fig. 4a, Fig. 4b and the online method in Fig. 4c, our model is much smaller without large quality loss. Compared with regularization-based and replay-based continual learning methods in Fig. 4d and Fig. 4e respectively, our method achieves significantly higher quality. Results of other scenes including depth maps are shown in Fig. 5.

4.3.2 Meetroom dataset.

Table 2 and Fig. 6 shows the quantitative and qualitative comparisons on the meetroom dataset. Fig. 7 is the PSNR curve of the compared methods on the *trimming* scene. As shown in Tab. 2, HexPlane-GR and HexPlane-PR fail and produce unsatisfactory results on the meetroom dataset, we thus exclude them from Fig. 7. Our method outperforms the implicit MLP-based online method [48] in terms of quality, speed, and model size significantly. Moreover, our method consumes only a fraction of storage than the explicit voxel-based online baseline [27] while maintaining comparable reconstruction quality as compared in

Fig. 6. When compared with offline baselines, our method produces comparable quality to MixVoxels [45] and outperforms HexPlane [7] in terms of quality and speed, and consumes much less memory as in Fig. 6. We use the released configuration of StreamRF [27] for the meetroom dataset. The *full model* of [27] results in much worse metrics than those reported in their paper, so we only report the metrics of their *pilot model*.

4.3.3 Spatial representations.

Our proposed continual learning framework is compatible with multiple spatial backbones. We provide quantitative results on hybrid representation (denoted as CD-MERF) and plane representation like [17, 21] (denoted as CD-Plane) on the DyNeRF dataset in Tab. 3. Since the element-wise product for plane representation in [17] produces unsatisfactory results due to the hash collision, we remove the $P_m(x, y, z)$ in Eq. (6) and fuse the features $Q_{mij}(i, j)$ by concatenation in the imple-

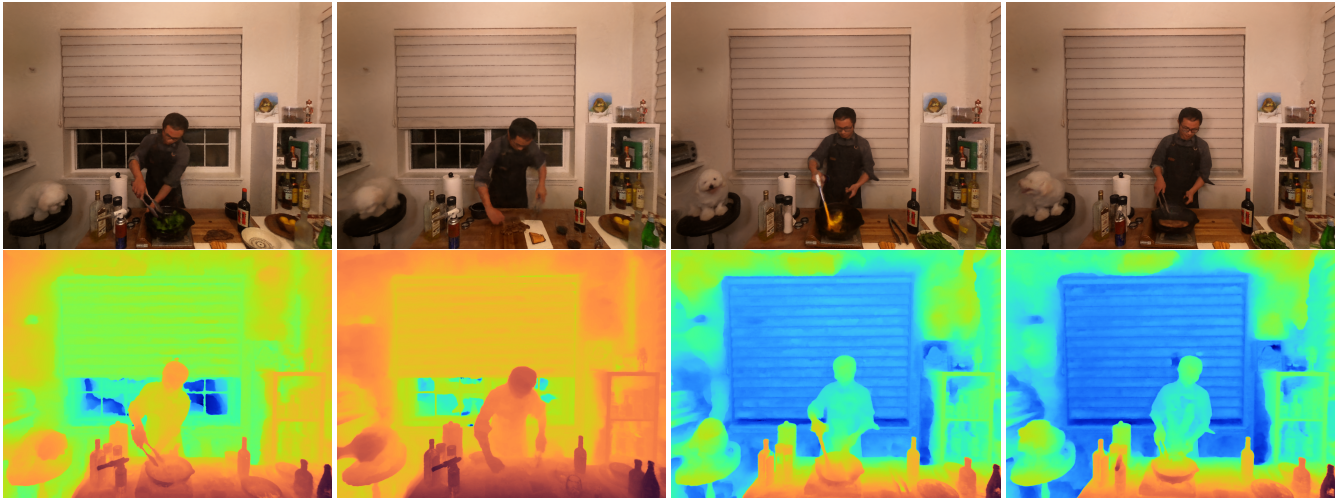


Fig. 5: The results of the proposed CD-NGP on DyNeRF dataset.

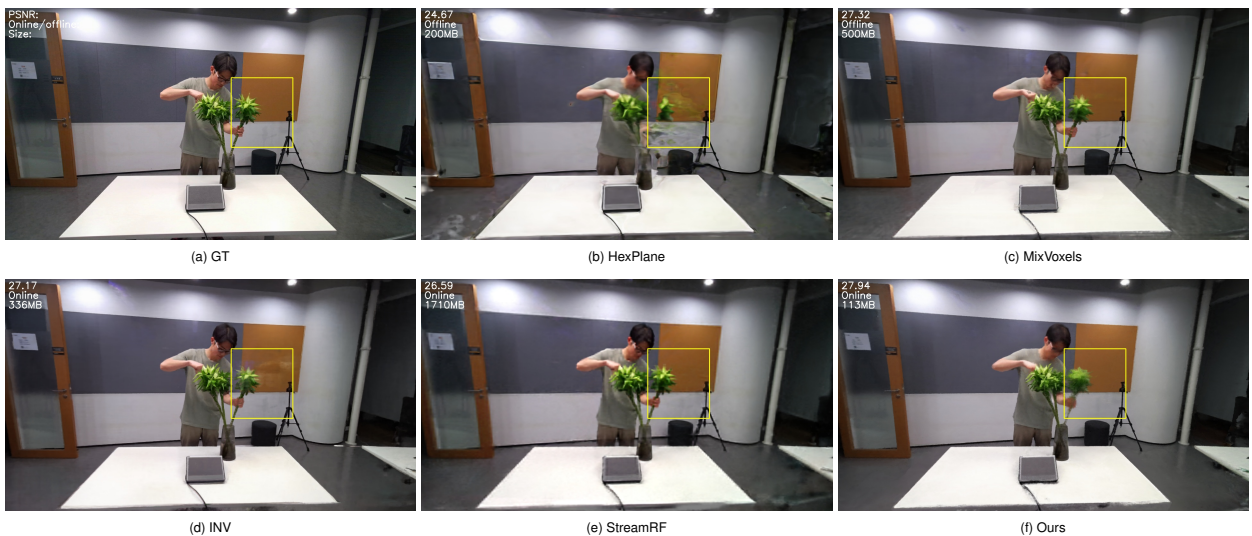


Fig. 6: Comparison of reconstruction quality on the *trimming* scene in the Meetroom dataset. Our method produces comparable quality to both offline and online state-of-the-art methods but with much less memory and storage cost.

mentation. We use 2^{P-2} -length hash tables for the *Plane* representation in Tab. 3 to balance the quality and the model size. The structural configurations (L, F) of the plane representation in Tab. 3 are set as (6, 4) for better results. The 3D+4D representation similar to [34] is yielded by concatenating the spatial (x, y, z) features and spatial-temporal (x, y, z, t) features encoded by a 4D extension of Eq. (5). By comparing our CD-NGP with the naive 3D+4D representation, we show the advantage of our asymmetric encoding of spatial-temporal (x, y, z, t) features explained in Eqs. (3) and (7): representing the features of spatial coordinates (x, y, z) and temporal coordinate (t) separately avoids feature collisions and lead to better results.

Table 3 also shows metrics of different feature fusion methods. We replace the element-wise sum in Eqs. (6) and (7) with vector concatenation and denote them as *CD-NGP-C* and *CD-MERF-C* in Tab. 3. The hybrid representations (*CD-MERF* and *CD-MERF-C*) achieve comparable model sizes (~ 60 MB) to methods for static scenarios [21, 31] without significant quality loss, reducing the average bandwidth cost to 0.2MB/frame. Benefiting from larger feature dimensions, the vector concatenation leads to slightly better quality (especially when measured in LPIPS) by more training time, and the reasonable trade-off also shows the robustness of our method. Compared with the hash table designs in Tab. 7, the *CD-NGP-C* representation in Tab. 3 almost per-

forms as well as the bulky (18, 18) configuration in Tab. 7 and reduces the model size by 80%. We list the per-scene results of the proposed continual learning method with different spatial representations on the DyNeRF dataset in Tab. 4.

The detailed parameter numbers and bandwidth consumption are listed in Tab. 5. *3D Enc.* and *2D Enc.* denote the spatial encodings along voxels and planes respectively. The tuples (M_1, M_2) in the cells denote the parameter numbers of the base encoder and each of the auxiliary encoders. Following [1, 27, 43, 48] we also report the minimum per-frame bandwidth consumption \mathbf{B}_{\min} , which only depends on the parameter numbers of the auxiliary branches and is thus significantly lower than the average bandwidth consumption \mathbf{B}_{avg} . Since the base encoder and the density grid could be shared among different branches and transmitted only once in the beginning, the minimum bandwidth consumption is reduced to 0.065 \sim 0.16 MB per frame, which is $100\times$ less than the voxel-based StreamRF [27] and $7\times$ less than the pure MLP representation INV [48].

4.3.4 Long sequence dataset and scalability analysis.

We also provide quantitative comparisons on our proposed long multi-view video dataset in Tab. 6 and Fig. 8 to further show the superior scalability of our method. We split the sequence into 300-frame chunks

Table 2: Results on the Meetroom dataset.

Method	Online	Offline	PSNR \uparrow	DSSIM \downarrow	LPIPS \downarrow	Time \downarrow	Size \downarrow
Mixvoxels		✓	26.96	0.027	0.1034	15min	500MB
HexPlane		✓	24.71	0.043	0.2206	100min	200MB
HexPlane-GR	✓		19.05	0.099	0.3999	100min	318MB
HexPlane-PR	✓		18.63	0.112	0.3589	100min	318MB
StreamRF	✓		26.48	0.029	0.1699	75min	1710MB
INV	✓		23.87	0.041	0.1195	40hours	336MB
CD-NGP (Ours)	✓		26.01	0.039	0.1906	77min	113MB

Table 4: Detailed results of the proposed CD-NGP and other hash-based methods on the DyNeRF dataset.

Model	Flame Salmon			Cook Spinach		
	PSNR \uparrow	DSSIM \downarrow	LPIPS \downarrow	PSNR \uparrow	DSSIM \downarrow	LPIPS \downarrow
CD-NGP	26.37	0.04586	0.2886	30.76	0.02440	0.1793
CD-NGP-C	26.65	0.04243	0.2680	31.03	0.02288	0.1593
CD-Plane	25.48	0.06058	0.3173	29.41	0.03487	0.2010
CD-MERF	26.15	0.04952	0.2921	30.35	0.02931	0.1858
CD-MERF-C	26.56	0.04435	0.2546	30.69	0.02609	0.1583
Model	Flame Steak			Sear Steak		
	PSNR \uparrow	DSSIM \downarrow	LPIPS \downarrow	PSNR \uparrow	DSSIM \downarrow	LPIPS \downarrow
CD-NGP	31.27	0.02132	0.1736	31.71	0.01917	0.1701
CD-NGP-C	31.64	0.01823	0.1403	32.02	0.01698	0.1424
CD-Plane	30.26	0.02949	0.1804	30.56	0.02723	0.1811
CD-MERF	31.01	0.02508	0.1719	31.44	0.02181	0.1698
CD-MERF-C	31.13	0.02424	0.1506	31.66	0.01989	0.1413
Model	Cut Roasted Beef			Average		
	PSNR \uparrow	DSSIM \downarrow	LPIPS \downarrow	PSNR \uparrow	DSSIM \downarrow	LPIPS \downarrow
CD-NGP	31.03	0.02366	0.1801	30.228	0.026882	0.19834
CD-NGP-C	31.26	0.02205	0.1578	30.520	0.024514	0.17356
CD-Plane	30.11	0.03302	0.1951	29.164	0.037038	0.21498
CD-MERF	30.71	0.02765	0.1856	29.932	0.030674	0.20104
CD-MERF-C	31.04	0.02450	0.1632	30.216	0.027814	0.17360

Table 5: The parameter numbers of each module of the 30-branch representations in Tab. 3. \mathbf{B}_{\min} and \mathbf{B}_{avg} are minimum and average bandwidth costs in MB/frame. # denotes the number of parameters per branch (10 frames).

Model	#3D Enc.	#2D Enc.	#MLP	#Online	#Total	\mathbf{B}_{\min}	\mathbf{B}_{avg}
CD-NGP	(9.9M, 0.37M)	-	0.042M	0.39M	21M	0.16	0.38
CD-NGP-C	(9.9M, 0.37M)	-	0.046M	0.40M	21M	0.16	0.38
CD-Plane	-	(1.9M, 0.082M)	0.048M	0.28M	14M	0.11	0.28
CD-MERF	(1.3M, 0.049M)	(0.56M, 0.023M)	0.042M	0.16M	7.5M	0.061	0.19
CD-MERF-C	(1.3M, 0.049M)	(0.56M, 0.023M)	0.052M	0.17M	7.5M	0.065	0.19

for the compared methods since the offline baseline [7] is designed for 300-frame sequences in the DyNeRF dataset. We set the hash table size as 2^{12} in the auxiliary branches and use $T_{\text{chunk}} = 5$ in our model. As shown in Tab. 6, our method reduces the memory and storage consumption by at least $4\times$ with comparable quality to HexPlane [7]. Compared with the results in Tab. 1, the performance gap in storage consumption is even larger in long video sequences. This is because the whole model shares one base branch and the following auxiliary branches occupy the majority of the parameters. We thus set the hash table size in the auxiliary branches to $2^{12}LF$ and leverage the re-use of the features from the base branch to reduce the model size to $\mathcal{O}(N_{\text{chunk}} \cdot 2^{12}LF)$.

The PSNR curves in Fig. 8 further demonstrate the stability of our method. The compared online methods suffer from *catastrophic forgetting*: the PSNRs at the beginning of the chunks are much lower than that in the end. The problem is properly eliminated by our method through parameter isolation, and our method continuously produce high-

quality results for the whole sequence. We also provide comparisons between the rendered results in Fig. 9. The regularization method displayed in Fig. 9a reconstructs the TV screen in the background erroneously. The replay method displayed in Fig. 9b fails to recover the details. Ours in Fig. 9f produces comparable quality to the offline baseline in Fig. 9c.

To further demonstrate the scalability of our method, we conduct experiments on the first 2400 frames of the *seminar* scene in our long video dataset, show the PSNR curves in Fig. 11 and compare the model sizes in Fig. 12. For simplicity of the evaluation, we set the chunk size as 10 for the CD-NGP and CD-MERF method. Our method produces high-quality results, and consumes only a fraction of storage space compared with the other online baselines.

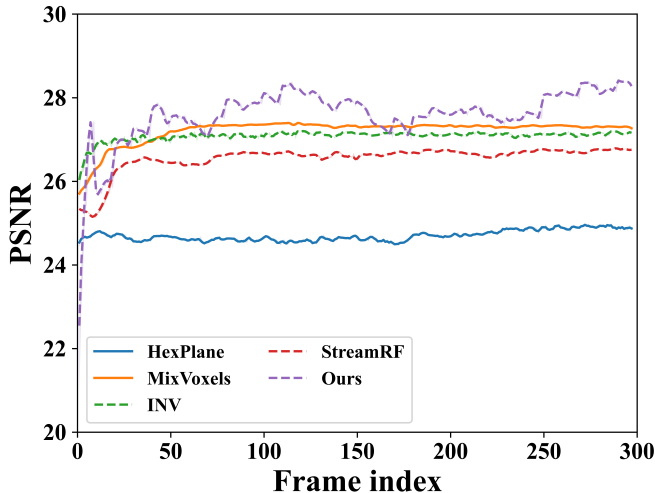


Fig. 7: PSNR curves of the compared methods on the *trimming* scene in the Meetroom dataset. Solid and dotted lines denote offline and online methods respectively.

Table 3: Ablation study on spatial representations. Different representations lead to subtle changes in quality metrics.

Model	Params	PSNR \uparrow	LPIPS \downarrow	Time \downarrow	Size \downarrow
CD-NGP	21M	30.23	0.198	75min	113MB
3D+4D	23M	29.34	0.243	82min	122MB
CD-NGP-C	21M	30.52	0.174	80min	114MB
CD-Plane	14M	29.16	0.215	77min	83MB
CD-MERF	7.5M	29.93	0.201	109min	57MB
CD-MERF-C	7.5M	30.22	0.174	115min	57MB

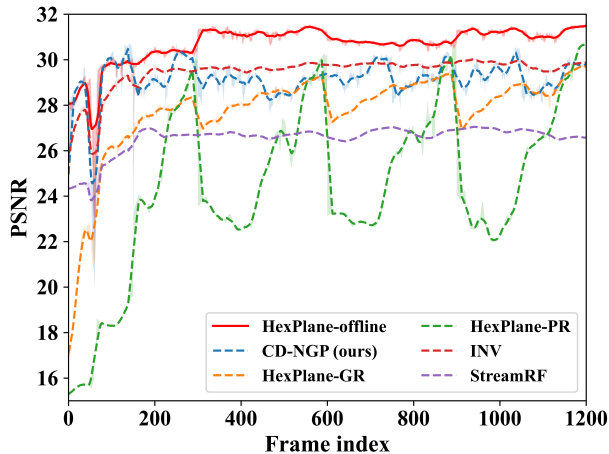


Fig. 8: PSNR curves of the first 1200 frames of *seminar* scene in our long video dataset. The solid lines and dotted lines denote offline and online methods respectively.

4.4 Ablation studies

4.4.1 Lengths of hash tables.

Benefiting from the multi-branch hash table design, our model is highly efficient and configurable. We change the parameter numbers of the initial branch and the auxiliary branches and obtain the results on the DyNeRF dataset in Tab. 7. (P_1, P_2) are the \log_2 values of the hash table lengths of the base branch and the other branches. Since

the whole model contains hash encoders, MLP regressors, and the occupancy grids. The sizes of the models are thus larger than the simple combinations of hash table and MLP regressors. We use the default configuration (19, 14) in the following experiments. Although larger hash tables alleviate hash collisions, the configuration (19, 14) in CD-NGP produces better results than the naive (16, 16) configuration even if the storage consumption is 40% lower. Moreover, the (19, 12) configuration of CD-NGP significantly outperforms the naive (14, 14) configuration at a similar storage cost. To further demonstrate the scalability of our method, we provide the PSNR curves of different hash table designs on the *sear steak* scene in Fig. 10. Equipped with a larger hash table in the base branch, the asymmetric setting (19, 14) and (19, 12) outperforms others in the beginning and produces comparable metrics to the naive (16, 16), (14, 14) configuration respectively in the subsequent chunks. The advantage comes from our asymmetric hash table designs: the base branch with a large hash table recovers more environment patterns, and the auxiliary branches could thus use fewer parameters to cope with recent changes only.

4.4.2 Temporal representations.

Our continual learning pipeline is also compatible with a variety of representations for the time axis. Currently, there are 2 other prevailing representations for the time axis alone: pure frequency encoding [36] and MLP with frequency-encoding [16]. We replace the temporal hash encoding in our method with the ones mentioned above on DyNeRF dataset and show the results in Tab. 8. Our time latent code slightly outperforms others on DyNeRF dataset. The robustness against changes in the temporal representations also shows the viability of the continual learning method.

4.4.3 Field composition methods.

We also conduct ablation studies on the field composition methods and show the results in Tab. 9 and Fig. 13. The field composition process is defined as:

$$(\sigma, \mathbf{c}) = (\sigma_i + \sigma_a, \mathbf{c}_i + \mathbf{c}_a). \quad (13)$$

Full composition in Tab. 9 denotes the naive composition of 2 fields from the base branch and the current branch respectively, *i.e.* σ_i and \mathbf{c}_i are the field from the base branch and σ_a and \mathbf{c}_a in Eq. (13) are the field from the current branch. Both branches are encoded with the same architecture as Eq. (3). *Static-dynamic* in Tab. 9 denotes a naive composition of the field from a static branch by the base encoder and a dynamic branch by the auxiliary encoders similar to [45], *i.e.* σ_i and \mathbf{c}_i in Eq. (13) are encoded without the $\Gamma(t)$ in Eq. (3). The online training strategies remain the same. Our CD-NGP outperforms the other methods in all metrics. Furthermore, as compared in Fig. 13, the compared composition methods in Figs. 13c and 13d suffer from salt and pepper noise because of the explicit composition, while our CD-NGP circumvents the problem by fusing features in the latent space and produces better results.

4.4.4 Regularization weights.

We also provide ablation studies on the regularization weights of auxiliary spatial encodings. We apply regularizations on $\Psi_k(x)$ with different λ_r and show the results in Tab. 10. The regularization is of slight improvement, and our method is robust within a wide range of λ_r .

4.4.5 Chunk size.

We also conduct ablation studies on the chunk sizes and show the results in Tabs. 11 and 12. We only report the results on the *cook spinach* scene in the DyNeRF dataset for brevity. Our method is robust within a wide range of chunk sizes. As in Tab. 11, the smaller chunk size leads to better results when controlling the iteration numbers of each chunk. When the total iterations of the whole 300-frame sequence are held constant, the larger chunk size leads to better results as in Tab. 12. We select $T_{chunk} = 10$ as the default configuration. The selection of the chunk size is a trade-off between the quality, robustness, training time, and host memory occupation and should depend on the data.

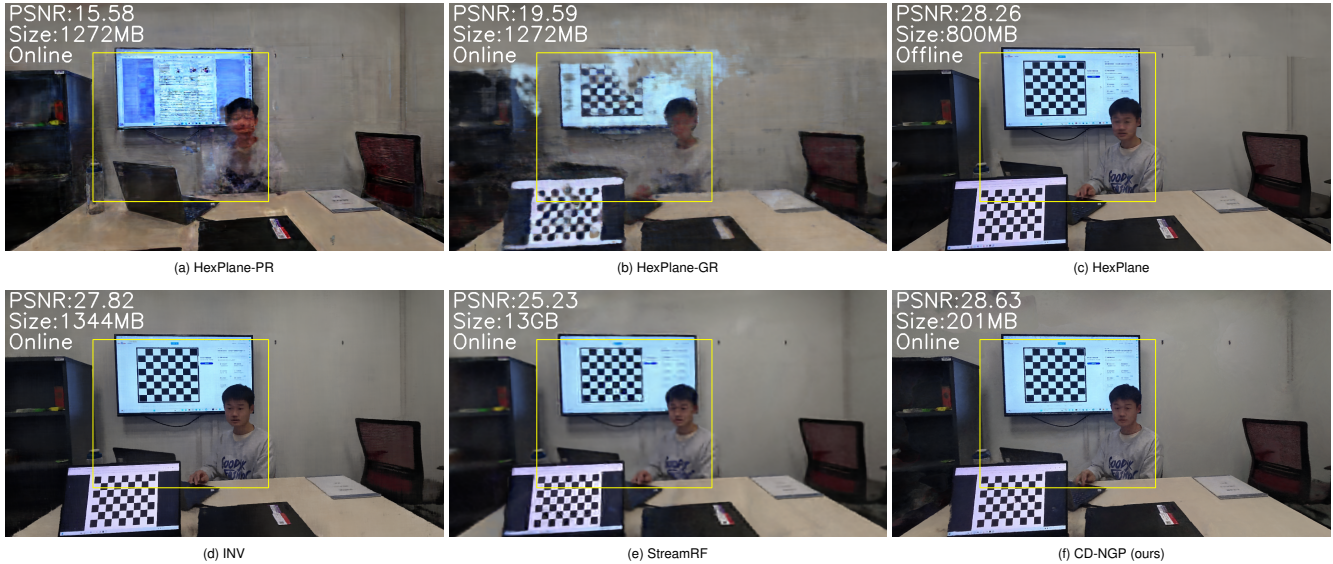


Fig. 9: Comparison of reconstruction quality on the 19th frame of the *seminar* scene in our long video dataset.

Table 6: Quantitative comparisons between our CD-NGP and baselines on the long video sequences in our dataset. Metrics are measured on the first 1200 frames and averaged among the different scenes. The compared HexPlane baselines are trained with a chunk size of 300 frames.

Method	Online	Offline	PSNR \uparrow	LPIPS \downarrow	Size \downarrow	Time \downarrow	Memory \downarrow
HexPlane		✓	28.32	0.117	800MB	8 hours	74GB
HexPlane-PR	✓		20.90	0.286	1272MB	8 hours	12GB
HexPlane-GR	✓		24.82	0.282	1272MB	8 hours	12GB
StreamRF	✓		24.99	0.266	13GB	4 hours	12GB
INV	✓		27.07	0.086	1344MB	160 hours	12GB
CD-NGP (Ours)	✓		27.15	0.190	201MB	10 hours	12GB

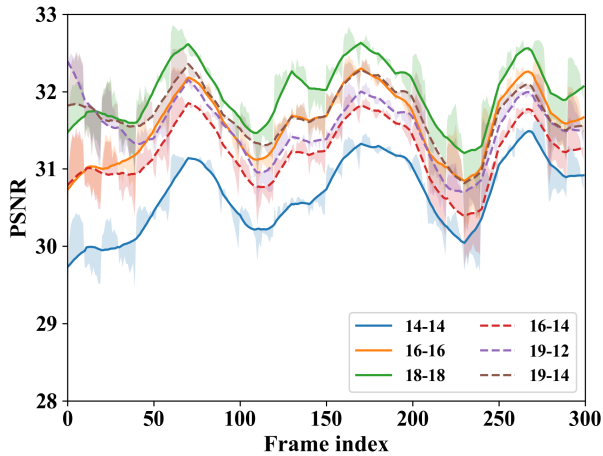


Fig. 10: PSNR curves of asymmetric (solid line, ours) and symmetric (dotted line) hash table designs on the *sear steak* scene.

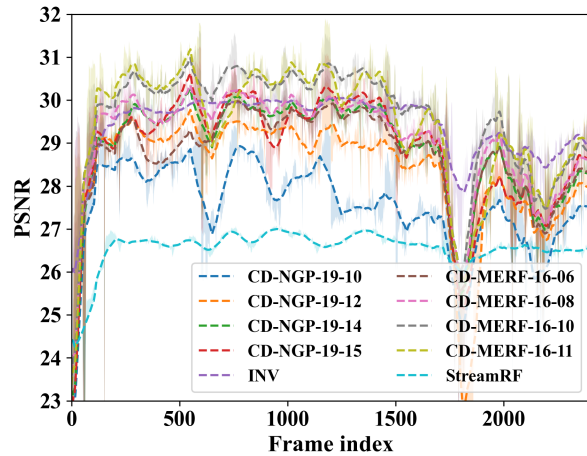


Fig. 11: PSNR curves of the first 2400 frames of *seminar* scene in our long video dataset.

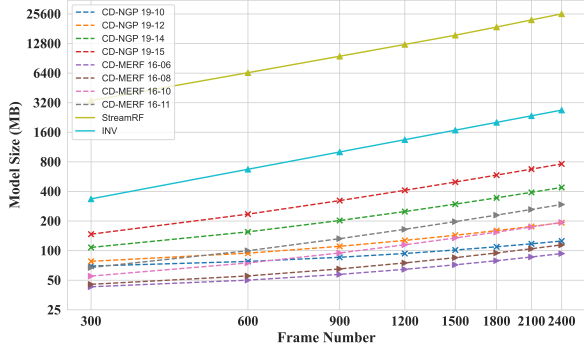


Fig. 12: Comparison of the model sizes of our method and other online baselines. Our method show superior scalability over the compared baselines.

Table 7: Ablation study on hash table sizes. † denotes the default setting.

(P_1, P_2)	Params	PSNR↑	Size↓
(18, 18)	151M	30.55	638MB
(16, 16)	41M	30.08	191MB
(14, 14)	12M	29.32	75MB
(19, 14)†	21M	30.23	113MB
(16, 14)	13M	29.78	79MB
(19, 12)	14M	30.09	82MB



Fig. 13: Comparison of different field composition methods.

5 CONCLUSION AND LIMITATION

We propose CD-NGP, a continual learning framework for multi-view dynamic scenes based on parameter isolation. Equipped with the multi-branch hash encoding structure, it shows high efficiency and scalability and is capable of reconstructing long video sequences with low host memory occupation. Compared with offline methods, it consumes 40% less bandwidth and 85% less memory than recent explicit baselines and achieves comparable quality while maintaining the speed advantage over the pure-MLP-based methods. Compared with online baselines, it significantly outperforms replay and regularization-based continual learning methods and reaches a new balance among reconstruction quality, training speed, bandwidth occupation, and memory cost. How-

Table 8: Ablation study on temporal representations.

Method	PSNR↑	DSSIM↓	LPIPS↓
CD-NGP	30.23	0.0269	0.198
Time-MLP	30.20	0.0273	0.202
Time-Freq	30.19	0.0272	0.203

Table 9: Ablation study on the field composition methods.

Method	PSNR↑	DSSIM↓	LPIPS↓
CD-NGP	30.23	0.0269	0.198
Full composition	29.24	0.0367	0.228
Static-dynamic	28.27	0.0568	0.291

Table 11: Ablation study on chunk sizes. The iteration numbers of each chunk are held constant under different T_{chunk} settings.

T_{chunk}	PSNR↑	DSSIM↓	LPIPS↓	Size↓
30	30.31	0.02654	0.1842	80MB
15	30.54	0.02557	0.1816	97MB
10	30.76	0.02440	0.1793	113MB
5	30.99	0.02268	0.1674	162MB

ever, like most of the NeRF-based methods, it still requires querying the field function and is not appropriate for achieving real-time rendering. Further efforts could be made to apply baking methods or Gaussian point clouds to continual learning to achieve real-time rendering in long video sequences for wide applications.

REFERENCES

- [1] B. Attal, J.-B. Huang, C. Richardt, M. Zollhoefer, J. Kopf, M. O’Toole, and C. Kim. Hyperreel: High-fidelity 6-dof video with ray-conditioned sampling. In *Proceedings of the IEEE/CVF Conference on Computer Vision and Pattern Recognition*, pp. 16610–16620, 2023. 2, 6, 7
- [2] J. T. Barron, B. Mildenhall, M. Tancik, P. Hedman, R. Martin-Brualla, and P. P. Srinivasan. Mip-nerf: A multiscale representation for anti-aliasing neural radiance fields. In *Proceedings of the IEEE/CVF International Conference on Computer Vision (ICCV)*, pp. 5855–5864, October 2021. 1
- [3] J. T. Barron, B. Mildenhall, D. Verbin, P. P. Srinivasan, and P. Hedman. Mip-nerf 360: Unbounded anti-aliased neural radiance fields. In *Proceedings of the IEEE/CVF Conference on Computer Vision and Pattern Recognition (CVPR)*, pp. 5470–5479, June 2022. 1, 4
- [4] J. T. Barron, B. Mildenhall, D. Verbin, P. P. Srinivasan, and P. Hedman. Zip-nerf: Anti-aliased grid-based neural radiance fields. *arXiv preprint arXiv:2304.06706*, 2023. 1
- [5] W. Bian, Z. Wang, K. Li, J.-W. Bian, and V. A. Prisacariu. Nope-nerf: Optimising neural radiance field with no pose prior. In *Proceedings of the IEEE/CVF Conference on Computer Vision and Pattern Recognition*, pp. 4160–4169, 2023. 1
- [6] Z. Cai and M. Müller. Clnrf: Continual learning meets nerf. In *Proceedings of the IEEE/CVF International Conference on Computer Vision*, pp. 23185–23194, 2023. 3
- [7] A. Cao and J. Johnson. Hexplane: A fast representation for dynamic scenes. *CVPR*, 2023. 1, 2, 3, 4, 5, 6, 8
- [8] J. Cao, H. Wang, P. Chemerys, V. Shakhrai, J. Hu, Y. Fu, D. Makoviichuk, S. Tulyakov, and J. Ren. Real-time neural light field on mobile devices. In *Proceedings of the IEEE/CVF Conference on Computer Vision and Pattern Recognition*, pp. 8328–8337, 2023. 2
- [9] A. Chen, Z. Xu, A. Geiger, J. Yu, and H. Su. Tensorf: Tensorial radiance fields. In *European Conference on Computer Vision*, pp. 333–350. Springer, 2022. 1, 2
- [10] Z. Chen, T. Funkhouser, P. Hedman, and A. Tagliasacchi. Mobilenerf: Exploiting the polygon rasterization pipeline for efficient neural field rendering on mobile architectures. In *Proceedings of the IEEE/CVF Conference on Computer Vision and Pattern Recognition*, pp. 16569–16578, 2023. 2

Table 10: Ablation study on regularization weight λ_r .

λ_r	PSNR \uparrow	DSSIM \downarrow	LPIPS \downarrow
10^{-5}	30.20	0.0269	0.198
10^{-4}	30.18	0.0268	0.196
10^{-3}	30.23	0.0269	0.198
10^{-2}	30.09	0.0279	0.197
1	29.66	0.0313	0.205

Table 12: Ablation study on chunk sizes. The total iterations of the whole 300-frame sequence are held constant under different T_{chunk} settings.

T_{chunk}	PSNR \uparrow	DSSIM \downarrow	LPIPS \downarrow	Size \downarrow
30	30.84	0.02392	0.1505	80MB
15	30.76	0.02413	0.1684	97MB
10	30.76	0.02440	0.1793	113MB
5	30.39	0.02602	0.2075	162MB

- [11] J. Chung, K. Lee, S. Baik, and K. M. Lee. Meil-nerf: Memory-efficient incremental learning of neural radiance fields. *arXiv preprint arXiv:2212.08328*, 2022. 3
- [12] M. De Lange, R. Aljundi, M. Masana, S. Parisot, X. Jia, A. Leonardis, G. Slabaugh, and T. Tuytelaars. A continual learning survey: Defying forgetting in classification tasks. *IEEE Transactions on Pattern Analysis and Machine Intelligence*, 44(7):3366–3385, 2022. doi: 10.1109/TPAMI.2021.3057446 3
- [13] K. Deng, A. Liu, J.-Y. Zhu, and D. Ramanan. Depth-supervised nerf: Fewer views and faster training for free. In *Proceedings of the IEEE/CVF Conference on Computer Vision and Pattern Recognition*, pp. 12882–12891, 2022. 1
- [14] P. Dhar, R. V. Singh, K.-C. Peng, Z. Wu, and R. Chellappa. Learning without memorizing. In *Proceedings of the IEEE/CVF conference on computer vision and pattern recognition*, pp. 5138–5146, 2019. 3
- [15] Y. Du, Y. Zhang, H.-X. Yu, J. B. Tenenbaum, and J. Wu. Neural radiance flow for 4d view synthesis and video processing. In *2021 IEEE/CVF International Conference on Computer Vision (ICCV)*, pp. 14304–14314. IEEE Computer Society, 2021. 1
- [16] J. Fang, T. Yi, X. Wang, L. Xie, X. Zhang, W. Liu, M. Nießner, and Q. Tian. Fast dynamic radiance fields with time-aware neural voxels. In *SIGGRAPH Asia 2022 Conference Papers*, pp. 1–9, 2022. 1, 2, 3, 9
- [17] S. Fridovich-Keil, G. Meanti, F. R. Warburg, B. Recht, and A. Kanazawa. K-planes: Explicit radiance fields in space, time, and appearance. In *Proceedings of the IEEE/CVF Conference on Computer Vision and Pattern Recognition*, pp. 12479–12488, 2023. 1, 2, 3, 5, 6
- [18] S. Fridovich-Keil, A. Yu, M. Tancik, Q. Chen, B. Recht, and A. Kanazawa. Plenoxels: Radiance fields without neural networks. In *CVPR*, 2022. 2
- [19] A. Gupta, J. Cao, C. Wang, J. Hu, S. Tulyakov, J. Ren, and L. A. Jeni. Lightspeed: Light and fast neural light fields on mobile devices. *arXiv preprint arXiv:2310.16832*, 2023. 2
- [20] P. Hedman, P. P. Srinivasan, B. Mildenhall, J. T. Barron, and P. Debevec. Baking neural radiance fields for real-time view synthesis. In *Proceedings of the IEEE/CVF International Conference on Computer Vision*, pp. 5875–5884, 2021. 2
- [21] W. Hu, Y. Wang, L. Ma, B. Yang, L. Gao, X. Liu, and Y. Ma. Tri-miprf: Tri-mip representation for efficient anti-aliasing neural radiance fields. In *Proceedings of the IEEE/CVF International Conference on Computer Vision*, pp. 19774–19783, 2023. 2, 3, 6, 7
- [22] B. Kerbl, G. Kopanas, T. Leimkühler, and G. Drettakis. 3d gaussian splatting for real-time radiance field rendering. *ACM Transactions on Graphics*, 42(4), 2023. 1, 2
- [23] D. P. Kingma and J. Ba. Adam: A method for stochastic optimization. *arXiv preprint arXiv:1412.6980*, 2014. 5
- [24] A. Krizhevsky, I. Sutskever, and G. E. Hinton. Imagenet classification with deep convolutional neural networks. In F. Pereira, C. Burges, L. Bottou, and K. Weinberger, eds., *Advances in Neural Information Processing Systems*, vol. 25. Curran Associates, Inc., 2012. 2, 5
- [25] Kwea. ngp_pl. https://github.com/kwea123/ngp_pl, 2022. 4, 5
- [26] A. Levy, M. Matthews, M. Sela, G. Wetzstein, and D. Lagun. Melon: Nerf with unposed images using equivalence class estimation. *arXiv preprint arXiv:2303.08096*, 2023. 1
- [27] L. Li, Z. Shen, Z. Wang, L. Shen, and P. Tan. Streaming radiance fields for 3d video synthesis. *Advances in Neural Information Processing Systems*, 35:13485–13498, 2022. 1, 3, 4, 5, 6, 7
- [28] T. Li, M. Slavcheva, M. Zollhöfer, S. Green, C. Lassner, C. Kim, T. Schmidt, S. Lovegrove, M. Goesele, R. Newcombe, and Z. Lv. Neural 3d video synthesis from multi-view video. In *Proceedings of the IEEE/CVF Conference on Computer Vision and Pattern Recognition (CVPR)*, pp. 5521–5531, June 2022. 1, 2, 3, 4, 5, 6
- [29] Z. Li, S. Niklaus, N. Snavely, and O. Wang. Neural scene flow fields for space-time view synthesis of dynamic scenes. In *Proceedings of the IEEE/CVF Conference on Computer Vision and Pattern Recognition*, pp. 6498–6508, 2021. 1
- [30] B. Mildenhall, P. P. Srinivasan, M. Tancik, J. T. Barron, R. Ramamoorthi, and R. Ng. Nerf: Representing scenes as neural radiance fields for view synthesis. In A. Vedaldi, H. Bischof, T. Brox, and J.-M. Frahm, eds., *Computer Vision – ECCV 2020*, pp. 405–421. Springer International Publishing, Cham, 2020. 1, 2, 3
- [31] T. Müller, A. Evans, C. Schied, and A. Keller. Instant neural graphics primitives with a multiresolution hash encoding. *ACM Transactions on Graphics (TOG)*, 41(4):1–15, 2022. 1, 2, 3, 4, 5, 7
- [32] M. Niemeyer, J. T. Barron, B. Mildenhall, M. S. Sajjadi, A. Geiger, and N. Radwan. Regnerf: Regularizing neural radiance fields for view synthesis from sparse inputs. In *Proceedings of the IEEE/CVF Conference on Computer Vision and Pattern Recognition*, pp. 5480–5490, 2022. 1
- [33] K. Park, U. Sinha, P. Hedman, J. T. Barron, S. Bouaziz, D. B. Goldman, R. Martin-Brualla, and S. M. Seitz. Hypernerf: A higher-dimensional representation for topologically varying neural radiance fields. *ACM Trans. Graph.*, 40(6), article no. 238, dec 2021. 1
- [34] S. Park, M. Son, S. Jang, Y. C. Ahn, J.-Y. Kim, and N. Kang. Temporal interpolation is all you need for dynamic neural radiance fields. In *Proceedings of the IEEE/CVF Conference on Computer Vision and Pattern Recognition*, pp. 4212–4221, 2023. 1, 2, 5, 6, 7
- [35] R. Po, Z. Dong, A. W. Bergman, and G. Wetzstein. Instant continual learning of neural radiance fields. In *Proceedings of the IEEE/CVF International Conference on Computer Vision*, pp. 3334–3344, 2023. 3
- [36] A. Pumarola, E. Corona, G. Pons-Moll, and F. Moreno-Noguer. D-nerf: Neural radiance fields for dynamic scenes. In *Proceedings of the IEEE/CVF Conference on Computer Vision and Pattern Recognition (CVPR)*, pp. 10318–10327, June 2021. 1, 2, 3, 9
- [37] C. Reiser, S. Peng, Y. Liao, and A. Geiger. Kilonerf: Speeding up neural radiance fields with thousands of tiny mlps. In *Proceedings of the IEEE/CVF International Conference on Computer Vision*, pp. 14335–14345, 2021. 2
- [38] C. Reiser, R. Szeliski, D. Verbin, P. Srinivasan, B. Mildenhall, A. Geiger, J. Barron, and P. Hedman. Merf: Memory-efficient radiance fields for real-time view synthesis in unbounded scenes. *ACM Transactions on Graphics (TOG)*, 42(4):1–12, 2023. 1, 3, 4, 5
- [39] T. Schaul, J. Quan, I. Antonoglou, and D. Silver. Prioritized experience replay. *arXiv preprint arXiv:1511.05952*, 2015. 3
- [40] R. Shao, Z. Zheng, H. Tu, B. Liu, H. Zhang, and Y. Liu. Tensor4d: Efficient neural 4d decomposition for high-fidelity dynamic reconstruction and rendering. In *Proceedings of the IEEE/CVF Conference on Computer Vision and Pattern Recognition*, pp. 16632–16642, 2023. 1
- [41] H. Shin, J. K. Lee, J. Kim, and J. Kim. Continual learning with deep generative replay. *Advances in neural information processing systems*, 30, 2017. 3
- [42] V. Sitzmann, S. Rezkikov, B. Freeman, J. Tenenbaum, and F. Durand. Light field networks: Neural scene representations with single-evaluation rendering. *Advances in Neural Information Processing Systems*, 34:19313–19325, 2021. 2
- [43] L. Song, A. Chen, Z. Li, Z. Chen, L. Chen, J. Yuan, Y. Xu, and A. Geiger. Nerfplayer: A streamable dynamic scene representation with decomposed neural radiance fields. *IEEE Transactions on Visualization and Computer Graphics*, 29(5):2732–2742, 2023. 1, 2, 3, 4, 5, 6, 7
- [44] C. Wang, B. Eckart, S. Lucey, and O. Gallo. Neural trajectory fields for dynamic novel view synthesis. *arXiv preprint arXiv:2105.05994*, 2021. 1
- [45] F. Wang, S. Tan, X. Li, Z. Tian, Y. Song, and H. Liu. Mixed neural voxels for fast multi-view video synthesis. In *Proceedings of the IEEE/CVF International Conference on Computer Vision*, pp. 19706–19716, 2023. 1, 2, 3, 4, 5, 6, 9
- [46] L. Wang, Q. Hu, Q. He, Z. Wang, J. Yu, T. Tuytelaars, L. Xu, and M. Wu. Neural residual radiance fields for streamably free-viewpoint videos. In

Proceedings of the IEEE/CVF Conference on Computer Vision and Pattern Recognition, pp. 76–87, 2023. 3

- [47] P. Wang, Y. Liu, Z. Chen, L. Liu, Z. Liu, T. Komura, C. Theobalt, and W. Wang. F2-nerf: Fast neural radiance field training with free camera trajectories. In *Proceedings of the IEEE/CVF Conference on Computer Vision and Pattern Recognition (CVPR)*, pp. 4150–4159, June 2023. 1
- [48] S. Wang, A. Supikov, J. Ratcliff, H. Fuchs, and R. Azuma. Inv: Towards streaming incremental neural videos. *arXiv preprint arXiv:2302.01532*, 2023. 1, 3, 5, 6, 7
- [49] G. Wu, T. Yi, J. Fang, L. Xie, X. Zhang, W. Wei, W. Liu, Q. Tian, and X. Wang. 4d gaussian splatting for real-time dynamic scene rendering. *arXiv preprint arXiv:2310.08528*, 2023. 2
- [50] X. Wu, J. Xu, X. Zhang, H. Bao, Q. Huang, Y. Shen, J. Tompkin, and W. Xu. Scanerf: Scalable bundle-adjusting neural radiance fields for large-scale scene rendering. *ACM Transactions on Graphics (TOG)*, 42(6):1–18, 2023. 1
- [51] Z. Xie, X. Yang, Y. Yang, Q. Sun, Y. Jiang, H. Wang, Y. Cai, and M. Sun. S3im: Stochastic structural similarity and its unreasonable effectiveness for neural fields. In *Proceedings of the IEEE/CVF International Conference on Computer Vision*, pp. 18024–18034, 2023. 1
- [52] D. Xu, Y. Jiang, P. Wang, Z. Fan, H. Shi, and Z. Wang. Sinnerf: Training neural radiance fields on complex scenes from a single image. In *European Conference on Computer Vision*, pp. 736–753. Springer, 2022. 1
- [53] G.-W. Yang, W.-Y. Zhou, H.-Y. Peng, D. Liang, T.-J. Mu, and S.-M. Hu. Recursive-nerf: An efficient and dynamically growing nerf. *IEEE Transactions on Visualization and Computer Graphics*, 2022. 1
- [54] Z. Yang, X. Gao, W. Zhou, S. Jiao, Y. Zhang, and X. Jin. Deformable 3d gaussians for high-fidelity monocular dynamic scene reconstruction. *arXiv preprint arXiv:2309.13101*, 2023. 2
- [55] Z. Yang, H. Yang, Z. Pan, and L. Zhang. Real-time photorealistic dynamic scene representation and rendering with 4d gaussian splatting. In *International Conference on Learning Representations (ICLR)*, 2024. 2, 5, 6
- [56] L. Yariv, P. Hedman, C. Reiser, D. Verbin, P. P. Srinivasan, R. Szeliski, J. T. Barron, and B. Mildenhall. Baked sdf: Meshing neural sdfs for real-time view synthesis. *arXiv preprint arXiv:2302.14859*, 2023. 1, 2
- [57] R. Zhang, P. Isola, A. A. Efros, E. Shechtman, and O. Wang. The unreasonable effectiveness of deep features as a perceptual metric. In *Proceedings of the IEEE conference on computer vision and pattern recognition*, pp. 586–595, 2018. 2, 5